AGU PUBLICATIONS

JGR

Journal of Geophysical Research: Space Physics

RESEARCH ARTICLE

10.1002/2017JA024260

Key Points:
- Vertical rise velocities of EPBs estimated from EAR observations are consistent with the nonlinear evolution of EPBs simulated by HIRB model
- The vertical rise velocities and maximum attainable altitudes of midnight EPBs are significantly smaller than those of postsunset EPBs
- Smaller rise velocities of midnight EPBs are due to both weak background zonal electric fields and reduced background ion density levels

Supporting Information:
- Movie S1
- Movie S2
- Movie S3
- Movie S4

Correspondence to:
S. Tulasi Ram,
tulasi@iigs.iigm.res.in

Citation:
Tulasi Ram, S., K. K. Ajith, T. Yokoyama, M. Yamamoto, and K. Niranjan (2017), Vertical rise velocity of equatorial plasma bubbles estimated from Equatorial Atmosphere Radar (EAR) observations and HIRB model simulations, *J. Geophys. Res. Space Physics*, *122*, 6584–6594, doi:10.1002/2017JA024260.

Received 13 APR 2017
Accepted 18 MAY 2017
Accepted article online 22 MAY 2017
Published online 5 JUN 2017
Corrected 3 JUL 2017

This article was corrected on 3 JUL 2017. See the end of the full text for details.

Vertical rise velocity of equatorial plasma bubbles estimated from Equatorial Atmosphere Radar (EAR) observations and HIRB model simulations

S. Tulasi Ram[1], K. K. Ajith[1], T. Yokoyama[2], M. Yamamoto[3], and K. Niranjan[4]

[1]Indian Institute of Geomagnetism, Navi Mumbai, India, [2]National Institute of Information and Communications Technology, Tokyo, Japan, [3]Research Institute for Sustainable Humanosphere, Kyoto University, Kyoto, Japan, [4]Department of Physics, Andhra University, Visakhapatnam, India

Abstract The vertical rise velocity (V_r) and maximum altitude (H_m) of equatorial plasma bubbles (EPBs) were estimated using the two-dimensional fan sector maps of 47 MHz Equatorial Atmosphere Radar (EAR), Kototabang, during May 2010 to April 2013. A total of 86 EPBs were observed out of which 68 were postsunset EPBs and remaining 18 EPBs were observed around midnight hours. The vertical rise velocities of the EPBs observed around the midnight hours are significantly smaller (~26–128 m/s) compared to those observed in postsunset hours (~45–265 m/s). Further, the vertical growth of the EPBs around midnight hours ceases at relatively lower altitudes, whereas the majority of EPBs at postsunset hours found to have grown beyond the maximum detectable altitude of the EAR. The three-dimensional numerical high-resolution bubble (HIRB) model with varying background conditions are employed to investigate the possible factors that control the vertical rise velocity and maximum attainable altitudes of EPBs. The estimated rise velocities from EAR observations at both postsunset and midnight hours are, in general, consistent with the nonlinear evolution of EPBs from the HIRB model. The smaller vertical rise velocities (V_r) and lower maximum altitudes (H_m) of EPBs during midnight hours are discussed in terms of weak polarization electric fields within the bubble due to weaker background electric fields and reduced background ion density levels.

Plain Language Summary Equatorial plasma bubbles are plasma density irregularities in the ionosphere. The radio waves passing through these irregular density structures undergo severe degradation/scintillation that could cause severe disruption of satellite-based communication and augmentation systems such as GPS navigation. These bubbles develop at geomagnetic equator, grow vertically, and elongate along the field lines to latitudes away from the equator. The knowledge on bubble rise velocities and their maximum attainable altitudes improves the accuracy of scintillation forecasting at latitudes away from the equator and helps in mitigating the errors in satellite-based augmentation systems.

1. Introduction

The equatorial plasma bubbles (EPBs) are generally nighttime equatorial *F* region phenomenon, characterized by density depletions in the ionospheric plasma. These plasma density irregularities with scale sizes ranging from few centimeters to several hundred kilometers are generated by a hierarchy of plasma instability processes. From the extensive studies during past several decades, the morphologies such as seasonal, local time, and solar activity variations of these EPB irregularities were grossly understood [*Chandra and Rastogi*, 1970; *Fejer et al.*, 1979; *Basu and Coppi*, 1999]. Understanding the day-to-day variability of this phenomenon has considerable practical importance today due to its impact on transionospheric radio communication systems. According to the present understanding, EPBs are developed at the bottomside *F* layer, through Rayleigh-Taylor instability mechanism [*Haerendel*, 1973] and grow nonlinearly to topside ionosphere via polarization electric field with in them [*Ossakow et al.*, 1979; *Tsunoda*, 1985; *Keskinen et al.*, 2003]. The steep vertical density gradient due to quick recombination of plasma after sunset and the rapid uplift of *F* layer via prereversal enhancement (PRE) of zonal electric field sets the conditions more favorable for the development of EPBs during the postsunset hours. However, from the previous studies, it is further confirmed that EPBs can freshly evolve even during the midnight hours. These EPBs are showing different morphological and dynamical features compared to the postsunset EPBs, and majority of them are observed during the June solstice of low solar active period [*Otsuka et al.*, 2009; *Yokoyama et al.*, 2011a; *Ajith et al.*, 2015; *Dao et al.*, 2016].

Once developed, the EPBs grow nonlinearly to higher altitudes and elongate along the magnetic flux tubes to either side of the dip equator. The maximum altitude that an EPB can grow determines the maximum latitude that these irregularities can map. When the EPB irregularities extended to the latitudes of equatorial ionization anomaly crest, they can cause strongest scintillation and severe degradation of transionospheric signals passing through that region [*Rama Rao et al.*, 2006]. Further the vertical rise velocity of EPBs determines the rate at which these irregularities can map to low latitudes away from the equator. Therefore, the maximum altitude (H_m) and the vertical rise velocity (V_r) are the two important parameters useful for improving the forecast of scintillation at low latitudes away from the equator.

Quite a few attempts are made to calculate the bubble rise velocity using different techniques like VHF radar [*Tsunoda*, 1981; *Tsunoda et al.*, 1982], spaced ionosonde technique [*Abdu et al.*, 1983], multistation scintillation observation [*Dabas and Reddy*, 1990], and by using numerical simulation [*Scannapieco and Ossakow*, 1976; *Ossakow et al.*, 1979]. From the radar observations of the plasma bubbles in the equatorial plane, it is shown that the rise velocities of the plasma bubbles vary from 125 to 350 m/s [*Tsunoda*, 1981; *Tsunoda et al.*, 1982]. From the observations of time and height of the spread *F* event at two spaced ionosonde stations, the vertical rise velocities of plasma bubbles over Brazilian region were estimated as 30 to 300 m/s by *Abdu et al.* [1983]. Using the multistation scintillation observations over Indian region, *Dabas and Reddy* [1990] showed that the bubble rise velocities vary from 15 to 416 m/s. *Yokoyama and Fukao* [2006] investigated the rise velocity of EPBs observed from Equatorial Atmosphere Radar (EAR) during postsunset hours and noted that the observed rise velocity is consistent with the nonlinear evolution of plasma bubbles as simulated by previous numerical studies.

In all the above studies, bubble rise velocity is estimated only for a limited number cases and the rise velocity calculation is limited only for postsunset EPBs. Recently, *Dao et al.* [2016] estimated the bubble rise velocities using Equatorial Atmosphere Radar (EAR) for both postsunset EPBs and the EPBs around midnight. They have reported that the rise velocities of midnight EPBs are significantly smaller compared to the postsunset EPBs. However, the factors responsible for the difference in the rise velocities between postsunset and midnight hours are not discussed in detail. In the present study, the maximum altitudes and vertical rise velocities of EPBs are estimated by observing the temporal and spatial evolution of EPBs from EAR during May 2010 to April 2013. The estimated rise velocities are compared with the nonlinear evolution of plasma bubbles under varying background conditions using high-resolution bubble (HIRB) model [*Yokoyama et al.*, 2014] to further understand the responsible factors for the differences in rise velocities between postsunset and midnight EPBs.

2. Estimation of Vertical Rise Velocity

In this study, the freshly evolved EPBs over Kototabang were selected based on their spatial and temporal evolution observed from the two-dimensional fan sector backscatter maps [*Ajith et al.*, 2015]. A total of 86 events were selected in which the EPBs with the signal-to-noise ratio larger than 0 dB continued for more than 10 min. In the present study, the EPBs which developed between 1800 and 2230 LT are considered as postsunset EPBs and those generated after 2230 LT as midnight EPBs. The vertical rise velocity and maximum altitudes of EPBs are estimated using the frame-by-frame analysis of fan sector backscatter maps at every 2 min intervals. Figure 1 presents the series of two-dimensional fan sector backscatter maps showing temporal and spatial evolution of EPB echoes during postsunset period as observed by EAR on 30 October 2012 (see Movie S1 provided under supporting information). It should be noted that the 16 beams of EAR are tilted by ~23–38° from zenith to meet the field line perpendicularity for optimum backscatter from the ~3 m scale irregularities. In the present analysis, we have mapped all the EAR observations to its apex locations for the estimation of maximum altitudes and vertical rise velocities. From Figure 1, a faint backscatter can be seen at an apex altitude of ~540 km at 1902 LT. It should be mentioned here that the EPB onset referred here corresponds to the time and locations at which the ~3 m scale field-aligned irregularities (FAI) were seen by EAR at their first appearance with detectable amplitude ($>$0 dB). As time progresses, the upward growth with increasing echo intensity of EPB can be observed from the successive backscatter echoes. The white contour line in each frame represents the signal-to-noise ratio that corresponds to 0 dB level. To estimate the vertical rise velocity, the top altitude of EPB echo with intensity $\geq$0 dB as marked by pink horizontal line is determined from the fan sector map for every 2 min intervals. These top altitude values are

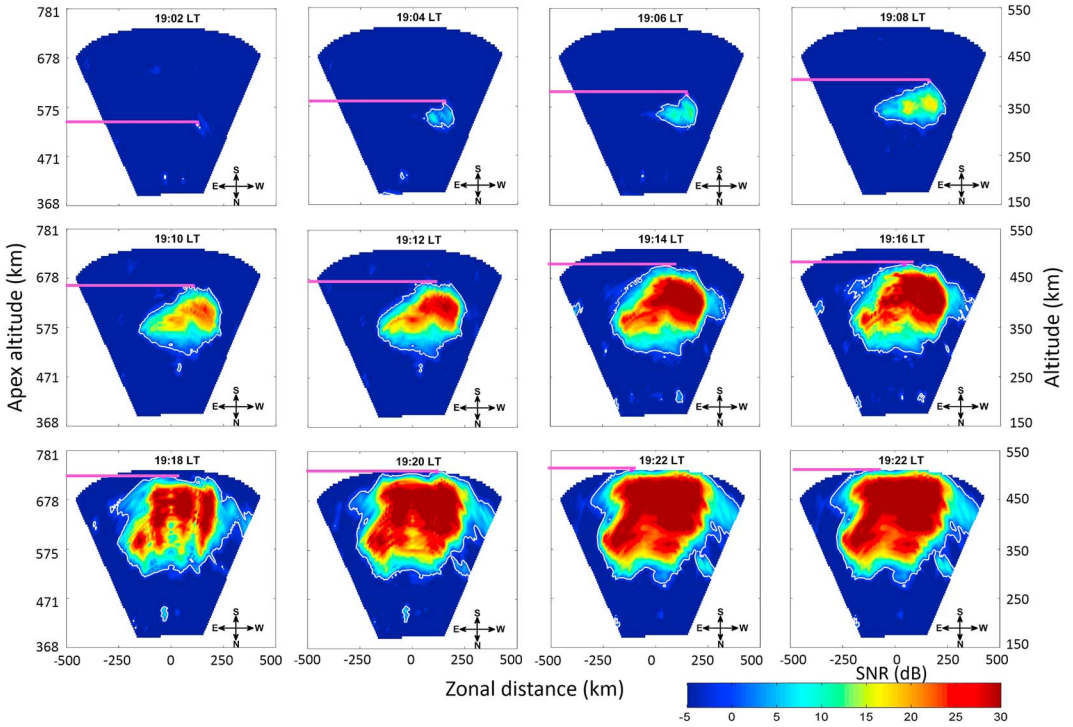

Figure 1. Time sequence of two-dimensional fan sector backscatter maps of the EPB (3 m scale FAI) echoes constructed from 16 beam observations of the EAR showing the spatial and temporal evolution of postsunset EPB on 30 October 2012 (see Movie S1).

noted during the growth phase until the EPB reaches the maximum detectable apex altitude (~740 km) of the radar, or EPB ceases to rise further in vertical direction, or EPB drifts out of the field of view (FOV) of the radar. From Figure 1 it can be seen that the top altitude of EPB echo (from ~3 m scale FAI) in the first frame (at 1902 LT) is 540 km. As the EPB growing vertically, it can also observed to be expanded eastward in the successive frames. The top altitude of EPB echo reached the maximum detectable altitude of 740 km at 1920 LT. Later, the EPB echo exhibited a large eastward drift and drifted completely out of the FOV (not shown in figure).

For example, Figure 2 shows the variation of top altitudes (represented by blue stars) of EPB echoes derived from successive fan sector maps shown in Figure 1 as a function of local time (see Movie S1). As can be seen in the figure, the top altitude rises quickly from 540 km to 740 km within 18 min (i.e., from 1902 to 1920 LT). Later, the EPB is further rising along with a significant zonal drift and the top altitude is beyond the maximum detectable altitude of the radar, hence, not determined. The slope of the linear fit (represented by the red dashed line) of echo top altitudes between 1902 and 1920 LT gives the mean vertical rise velocity of EPB during its nonlinear evolution phase which is estimated as 181 m/s. Similarly, Figures 3 and 4 show the spatial and temporal evolution of a midnight EPB and its top altitude variation with local time, respectively, observed on 22 July 2011 (see

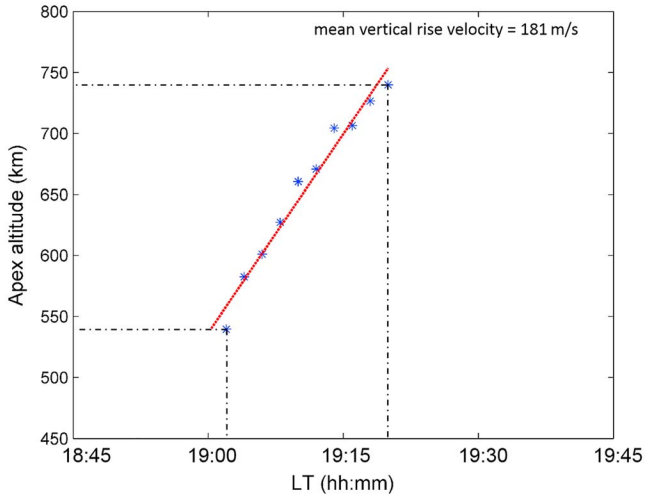

Figure 2. The vertical rise velocity estimation for the postsunset EPB shown in Figure 1 (see Movie S1).

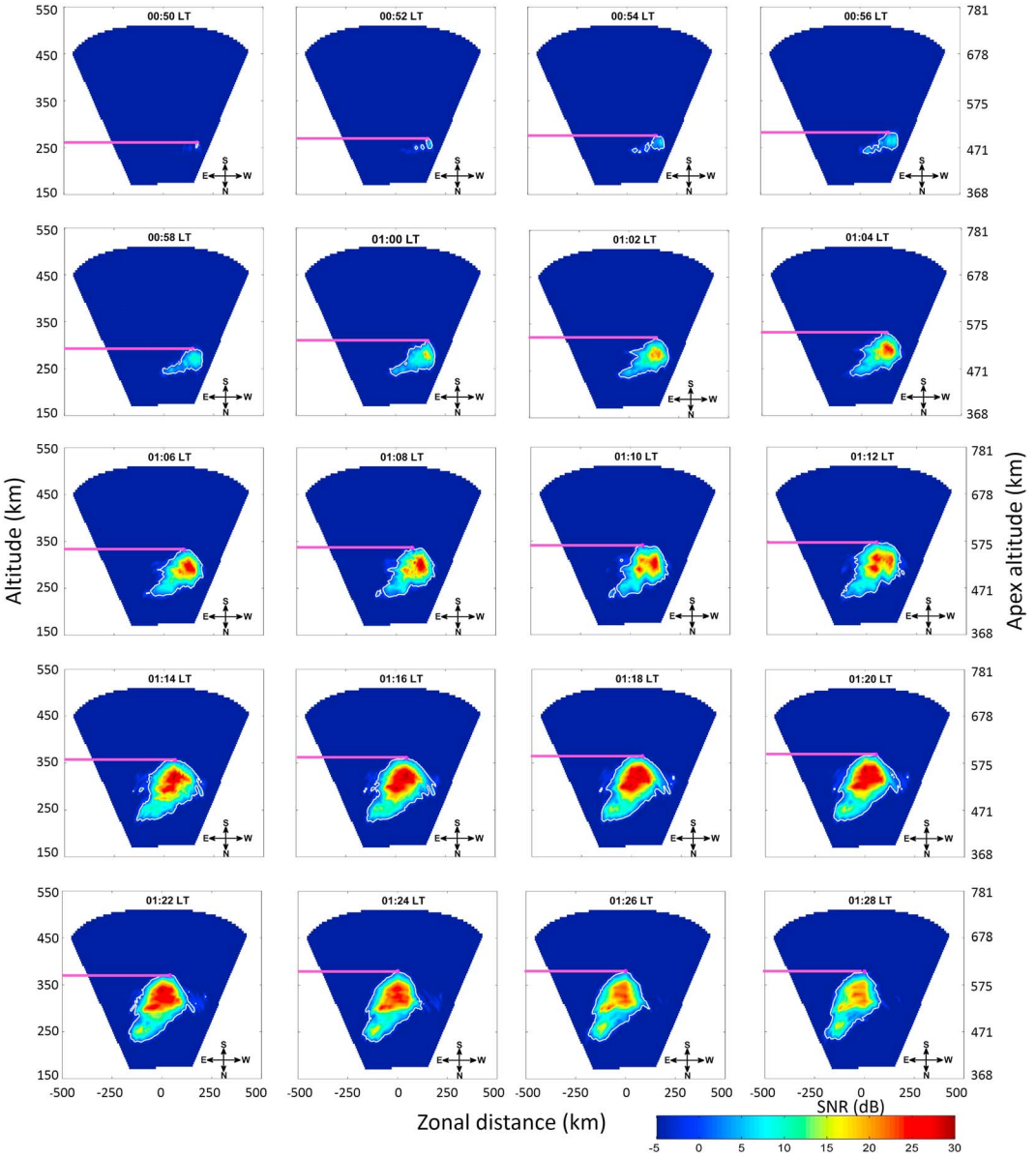

Figure 3. Time sequence of two-dimensional fan sector backscatter maps of the EPB echoes constructed from 16 beam observations of the EAR showing the spatial and temporal evolution of midnight EPB on 22 July 2011 (see Movie S2).

Movie S2). From Figure 3, it can be observed that a faint backscatter is observed at 0050 LT around ~482 km apex altitude. The top altitude of EPB echo in Figure 4 increases from 482 km at 0050 LT to 604 km at 0126 LT and remains more or less at the same altitude at later period. The mean vertical rise velocity estimated by linear fit of echo top altitudes between 0050 and 0126 LT is 58 m/s, which is significantly smaller compared to the postsunset EPB shown in Figures 1 and 2.

Following the similar method, the vertical rise velocities (V_r) of a total of 86 EPBs considered in this study were estimated and presented in Figure 5a as a function of local time. Out of 86 EPBs, 68 are from postsunset period represented by black circles and 18 EPBs (indicated by red circles) were observed around midnight hours. The black and red solid curves in Figure 5a indicate the variation of mean rise velocity with local time with the standard deviation shown as error bars. From Figure 5a, it can be seen that the rise velocities of postsunset EPBs exhibit large variability from ~45 to 265 m/s. The rise velocities of postsunset EPBs are significantly large just after sunset and rapidly decreases with local time and reaches a minimum around 2100 LT. The large values of V_r after the sunset are mainly due to prereversal enhancement (PRE) in the background zonal

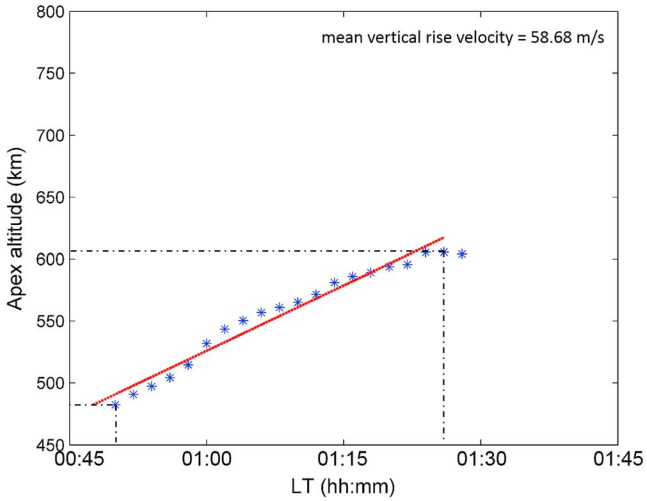

Figure 4. The vertical rise velocity estimation for the midnight EPB shown in Figure 3 (see Movie S2).

electric field and the resultant elevation of equatorial *F* layer which in turn enhances growth rate because of the decrease in ion-neutral collision frequency. The rapid decrease in V_r at later times is mainly due to the decrease in the zonal electric field and the consequent downward drift of equatorial *F* layer. On the other hand, the rise velocities of midnight EPBs are smaller than those of postsunset EPBs and found to vary between ~26 and 128 m/s. As we already discussed, the maximum altitude (H_m) reached by an EPB determines the maximum latitude that these irregularities can map. Figure 5b shows the maximum altitude (H_m) of total 86 EPBs as a function of local time. The black and red circles represent the postsunset and midnight EPBs, respectively. It can be observed from Figure 5b that around 55% (38 EPBs) of postsunset

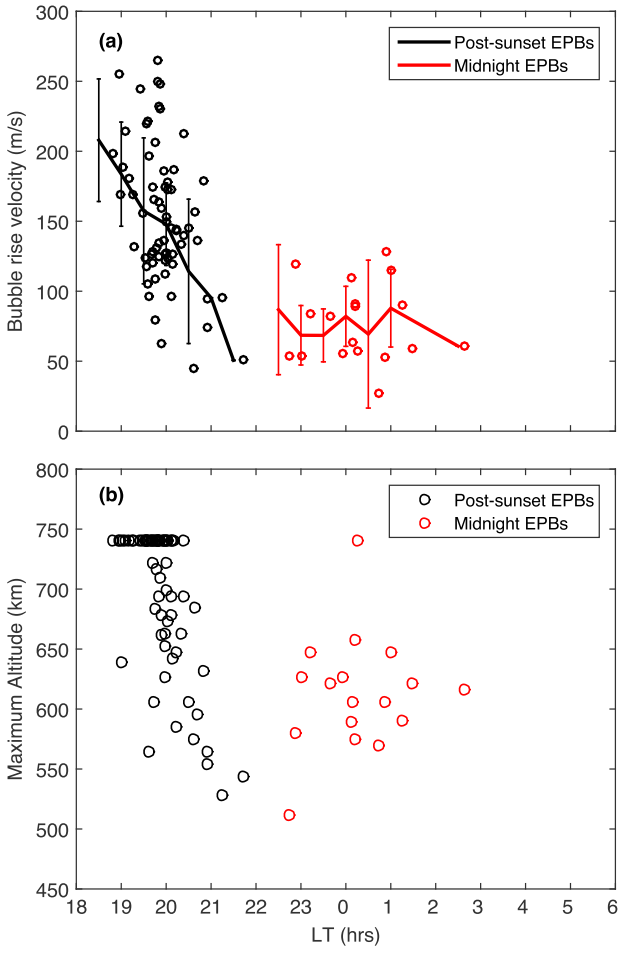

Figure 5. Local time variation of the (a) vertical rise velocity (V_r) and (b) maximum attainable altitude (H_m) of postsunset (black circles) and midnight (red circles) EPBs observed from the EAR.

EPBs have raised up to/beyond the maximum detectable altitude (740 km) of radar. The rest of 45% postsunset EPBs have ceased in further vertical rise after certain time and/or exhibited large eastward drift and eventually drifted out of the radar FOV. The maximum altitude (H_m) of these postsunset EPBs also decreases with local time and reaches minimum value around 2100 LT. On the other hand, the H_m attained by the EPBs around midnight hours are lower compared to the postsunset EPBs.

3. High-Resolution Bubble (HIRB) Model Simulations

The higher bubble rise velocities observed during the postsunset period (Figure 5a) can be expected as the result of higher background zonal electric field due to PRE [*Abdu et al.*, 1983; *Dabas and Reddy*, 1990]. Similarly, the slower rise velocities of EPBs around midnight hours could be due to weak background electric field and/or smaller background plasma densities around those local times. With a view to examine the effects of background zonal electric field and plasma density on the vertical rise velocity of EPBs during postsunset and midnight periods, the high-resolution bubble (HIRB) model [*Yokoyama et al.*, 2014] simulations have been carried out with varying background conditions.

The high-resolution bubble (HIRB) model uses the magnetic dipole coordinate system for equatorial and low-latitude ionosphere and covers 88–1270 km altitude range over the geomagnetic equator. The latitude coverage is ±20°, and longitudinal domain is 3.4° with periodic boundary condition, which indicates that a small local time variation within this longitude bin is ignored. The model considers a total of 851 magnetic field lines in the said altitude range, and each field line is divided into 501 grid points. The lower boundary is set at 80 km altitude. The number of grid points in longitude direction is 341. That means, the spatial resolution perpendicular to the magnetic field line is nearly 1.1 km (0.01° in longitude), which enables the HIRB model to reproduce the bifurcation and turbulent structure of EPB. The atmospheric and ionospheric parameters are obtained from International Reference Ionosphere (IRI) and Naval Research Laboratory Mass Spectrometer and Incoherent Scatter radar Exosphere 2000 (NRLMSISE-00) models. In the present study, the HIRB model simulations were carried out under both postsunset and midnight conditions with varying background zonal electric field inputs over Southeast Asian sector centered on 100°E longitude. The electric fields are set to different constant values between 250 km and 400 km and exponentially decay above and below. For all the cases, a LSWS (large-scale wave structure)-type initial seeding is applied with a wavelength of 2.4° in longitude (267 km), and the amplitude is about 10 km above the equator [see *Yokoyama et al.*, 2014].

3.1. Case 1: Postsunset Hours With Varying Zonal Electric Fields

In this case, the HIRB model simulations were carried out at postsunset local time (1930 LT) conditions with the background zonal electric field (E) set to 1 mV/m and 0.5 mV/m, which corresponds to approximately ~27 m/s and 15 m/s of postsunset vertical drift over this (100°E) sector. Figures 6a and 6b show the time evolution of EPB from HIRB simulation on zonal distance (longitude) and altitude plane over the magnetic equator with 1 mV/m and 0.5 mV/m background zonal electric fields, respectively, under postsunset local time conditions. The time elapsed from the beginning of the simulation is indicated at the top of each panel.

From Figure 6a, one can see the onset of an EPB from the crest of an upwelling at $T = 900$ s. The top altitude of this initial EPB is noted to be ~400 km as indicated by the red horizontal marker line. As the time progresses, the EPB has grown successively in to a more turbulent structure and exhibits pinching from the westward wall of EPB. In this figure, the successive frames showing temporal and spatial evolution of EPB structure are presented at 300 s interval for simplicity. The right-hand side panel (scatterplot) shows the variation of top altitude of the EPB structure as a function of time at every 100 s intervals. The slope of the linear fit gives the mean velocity of 264 m/s. Figure 6b shows the results of HIRB simulation with the reduced zonal electric field ($E = 0.5$ mV/m) input (see Movie S3). Two important observations that can be made from this figure are (i) the bubble onset is delayed and occurred at $T = 1500$ s and (ii) the mean vertical rise velocity is decreased to 226 m/s. This indicates that the bubble onset is delayed and the rise velocity becomes slower with the decrease in background zonal electric field from $E = 1$ mV/m to 0.5 mV/m. Nevertheless, the derived vertical rise velocities from the HIRB model are in similar range and consistent with the rise velocities derived from the EAR observations during postsunset hours shown in Figure 5a.

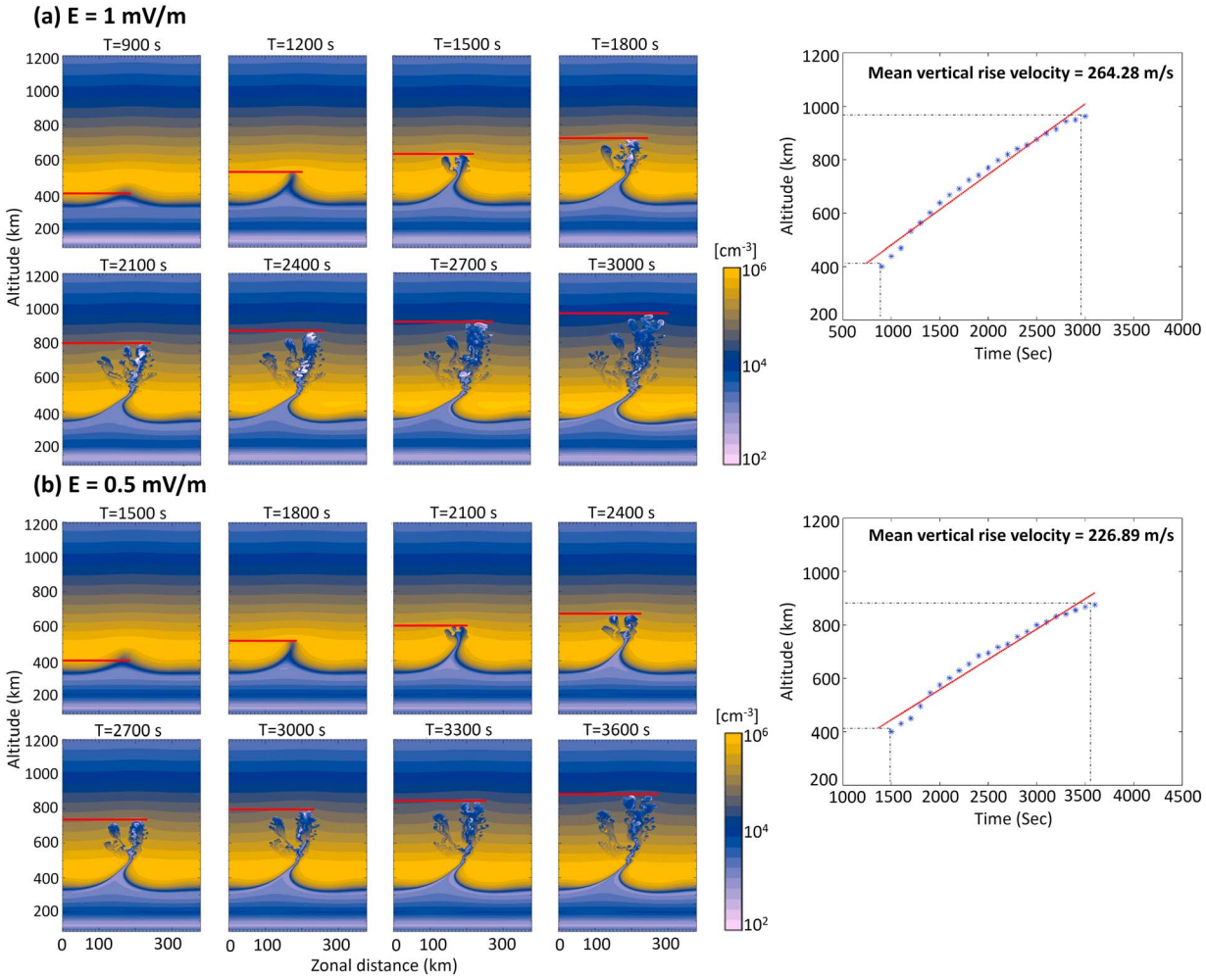

Figure 6. The time evolution of EPB from HIRB simulation on longitude and altitude plane over the magnetic equator under postsunset local time conditions with background zonal electric field of (a) 1 mV/m and (b) 0.5 mV/m, respectively. The right-hand side panel (scatterplot) showing the variation of top altitude of the EPB structure as a function of time at every 100 s intervals. (see Movie S3 for the case shown in Figure 6b).

3.2. Case 2: Midnight Hours With Varying Zonal Electric Fields

Figures 7a and 7b are similar to those of Figures 6a and 6b, except for midnight local time (0000 LT) conditions with background zonal electric fields that are set to 0.5 mV/m and 0.1 mV/m, respectively. It can be observed from Figure 7a that the bubble onset is occurred at T = 2300 s and the rise velocity is ~183 m/s for the case of E = 0.5 mV/m with the reduced background ionization levels during midnight. That means the bubble onset during midnight is delayed by ~800 s and the rise velocity is lowered by ~43 m/s compared to the postsunset conditions for the same background E = 0.5 mV/m (Figure 6b). This suggests that the background ion density also significantly influences the bubble rise velocity in addition to the zonal electric field.

Figure 7b shows the evolution of plasma bubble under midnight conditions with very small background electric field (E = 0.1 mV/m) (see Movie S4). *Stoneback et al.* [2011] and *Ajith et al.* [2016] have shown that the vertical $E \times B$ drifts over Southeast Asian sector around midnight are close to zero and sometimes can be slightly positive from the Ion Velocity Meter observations on board the Communication/Navigation Outage Forecasting System satellite. Hence, E = 0.1 mV/m is a more appropriate value under midnight local time conditions around this sector. From Figure 7b, it can be observed that the bubble onset is significantly delayed and occurred at T = 4800 s. The bubble rise velocity is also substantially slower, i.e., approximately 118 m/s. Nevertheless, the derived rise velocity of 118 m/s is consistent with the rise velocities derived from the EAR observations (~26–128 m/s) around midnight hours (Figure 5a).

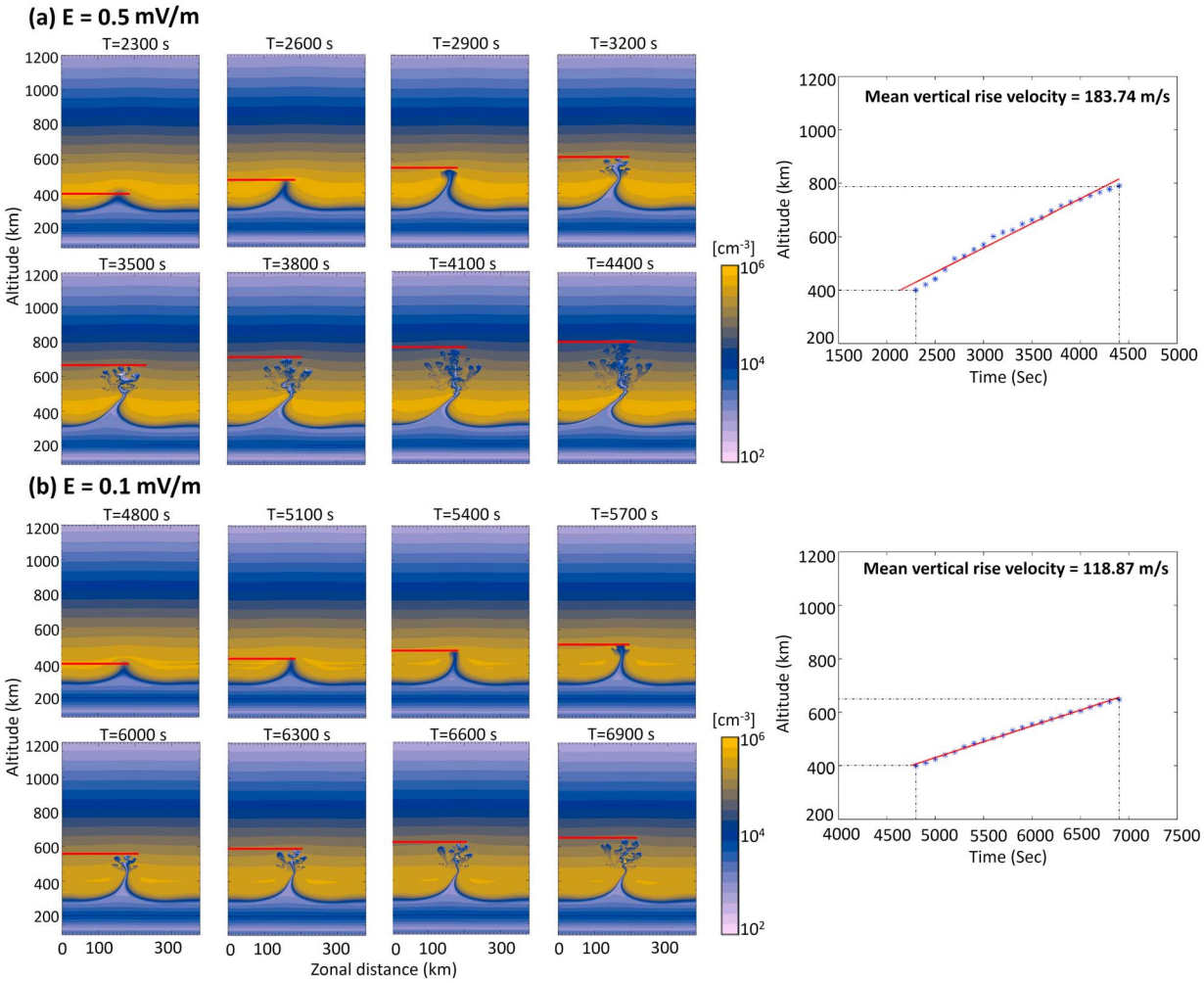

Figure 7. The time evolution of EPB from HIRB simulation on longitude and altitude plane over the magnetic equator under midnight local time conditions with background zonal electric field of (a) 0.5 mV/m and (b) 0.1 mV/m, respectively. The right-hand side panel (scatterplot) showing the variation of top altitude of the EPB structure as a function of time at every 100 s intervals. (see Movie S4 for the case shown in Figure 7b).

4. Discussion

The equatorial plasma bubbles are initiated at the bottomside *F* layer via polarization electric fields induced across the perturbation in the Pedersen conductivity. This perturbation in the Pedersen conductivity is generally thought to be developed due to gravity wave activity (gravity wave seeding) from the lower atmospheric origin and subsequent development of bottomside zonal large-scale wave structure (LSWS) in ion density [*Tsunoda and White*, 1981; *Tsunoda*, 2005; *Tsunoda et al.*, 2011; *Tulasi Ram et al.*, 2012; *Tulasi Ram et al.*, 2014]. The eastward polarization electric field induced in the depleted region (low-conductivity region) pushes the low-density plasma upward via $E \times B$ drift, and the plasma bubble initially develops at the bottomside *F* layer through Rayleigh-Taylor (RT) instability. The linear growth rate of RT instability depends on several factors such as the elevated height of the *F* layer, ion-neutral collision frequency, field-line-integrated conductivities, and the altitude of steep vertical density gradient region [*Sultan*, 1996; *Yizengaw et al.*, 2013; *Carter et al.*, 2014; *Ajith et al.*, 2016]. The strong eastward electric field due to prereversal enhancement (PRE) during the postsunset hours causes rapid uplift of equatorial *F* layer and sets the most favorable conditions for the development of EPBs [*Basu et al.*, 1996; *Fejer et al.*, 1999; *Fagundes et al.*, 1999; *Tulasi Ram et al.*, 2006].

Besides the seeding, development of LSWS, and the onset of bubble, the low-density plasma within the bubble grows nonlinearly and penetrates to higher altitudes. The steep upward density gradients at the walls of the bubble become more unstable, and the secondary instabilities cause the development of smaller-scale

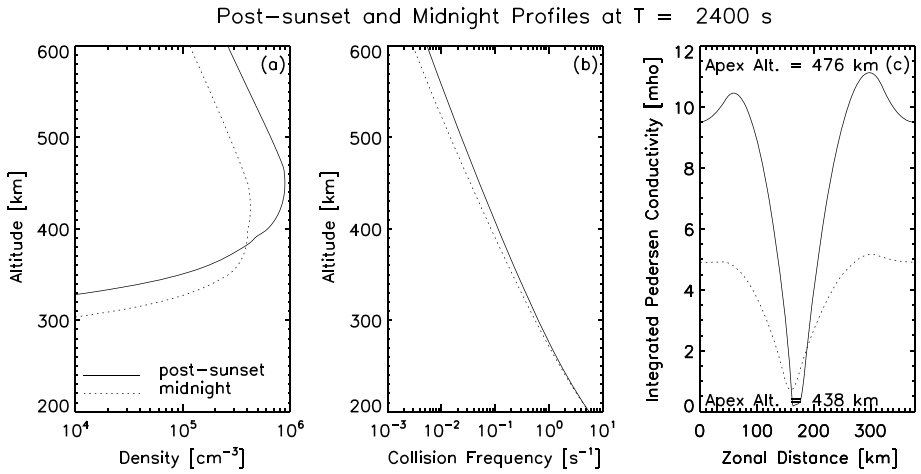

Figure 8. (a) Vertical ion density profiles, (b) ion-neutral collision frequency, and (c) horizontal variation (zonal cut) of flux tube integrated Pedersen conductivity for postsunset (solid curves) and midnight (dashed curves) cases with the same background zonal electric field of E = 0.5 mV/m presented in Figures 6b and 7a, respectively. Profiles shown in this figure correspond to the initial stage of bubbles at T = 2400 s from the beginning of HIRB simulation.

irregularities and turbulent plume-like structures in the topside. Therefore, the vertical rise velocities estimated in the present study represent the nonlinear growth phase of EPBs. From the EAR observations, the rise velocities of the postsunset EPBs estimated in 68 cases were found to vary between 45 and 265 m/s, whereas the midnight EPBs in 18 cases vary from 26 to 128 m/s. These estimated rise velocities from EAR observations are further found to be consistent with the three-dimensional, numerical high-resolution bubble (HIRB) model. The controlled HIRB simulations show that the rise velocity varies from 264 m/s to 227 m/s during postsunset hours when the background electric field varied from 1 mV/m to 0.5 mV/m, respectively. This indicates that the vertical rise velocity (nonlinear growth) of EPBs is significantly controlled by the background zonal electric field.

Using theoretical modeling, *Anderson and Haerendel* [1979] reported that the bubble rise velocities are, in general, small (large) when the *F* region ambient zonal electric field is small (large). *Abdu et al.* [1983] suggested that the background zonal electric field can affect the EPB rise velocity in two ways: first, through polarization changes resulting from the difference in the conductivity between the bubble and nearby regions due to the presence of background zonal electric field and second, through the uplift of *F* layer to higher altitudes where the EPB growth rate becomes higher due to reduced ion-neutral collision frequency. Later, *Dabas and Reddy* [1990] showed that the bubble rise velocity increases with the increase in the postsunset vertical drift of *F* layer and found that the EPB rise velocity is higher when the base height ($h'F$) of equatorial *F* layer is elevated.

Around midnight hours, background electric field (E) is expected to be westward [*Fejer et al.*, 1991], which causes a downward $E \times B$ drift. However, it has been observed that the background electric field during the midnight hours is generally weak or sometimes turns to eastward over this sector, particularly, during the June solstices of low solar activity periods [*Fejer et al.*, 1991; *Stoneback et al.*, 2011; *Ajith et al.*, 2016]. Further, few reports indicate that equatorial *F* layer is often elevated prior to the development of midnight EPBs [*Subbarao and Krishna Murthy*, 1994; *Sastri*, 1999; *Ajith et al.*, 2015]. The possible mechanisms for the elevated *F* layer and development of EPBs around midnight hours can be found elsewhere [*Yokoyama et al.*, 2011a, 2011b; *Dao et al.*, 2016 and *Ajith et al.*, 2016] which is beyond the scope of the current paper. Besides the development, the EPBs around midnight exhibit significantly slower rise velocities compared to postsunset hours due to weak or reduced background electric fields. The controlled HIRB simulations further show that the rise velocity decreases to 183 m/s during midnight hours (Figure 7a) compared to 227 m/s at postsunset hours (Figure 6b) for the same background zonal electric field of 0.5 mV/m. This indicates that the background ion density also influences the vertical rise velocity of the EPBs. Hence, the significantly smaller rise velocities observed around midnight hours can be attributed to both the factors of reduced background electric field and ion densities.

The Pedersen conductivity at *F* region altitudes is proportional to the background ion density and ion-neutral collision frequency [*Hargreaves*, 1992; *Baumjohann and Treumann*, 1997]. The reduced background ion density around the midnight hours causes smaller Pedersen conductivity gradient between the bubble and the adjacent regions that result in smaller induced polarization fields within the bubble. With a view to examine the role of background ion density on the conductivity gradient, the background ion density profiles for postsunset (solid curve) and midnight (dashed curve) are shown in Figure 8a for the cases presented in Figures 6b and 7a with the same zonal electric field, $E = 0.5$ mV/m. Here the background ion density profiles were taken outside the bubble region during the initial stage at $T = 2400$ s from the beginning of the HIRB simulation. Figure 8b shows the corresponding altitudinal variations of ion-neutral collision frequency, and Figure 8c shows the horizontal variation (zonal cut) of flux tube-integrated Pedersen conductivity at F_2 layer peak altitudes across the bubble. It can be observed from Figure 8c that the Pedersen conductivity is large for postsunset case (solid curve) and exhibits a large horizontal gradient between the bubble and the adjacent regions. However, the Pedersen conductivity during midnight (dashed curve) is small and exhibits relatively smaller gradient. The small (large) horizontal gradient in Pedersen between the bubble and adjacent regions results in smaller (larger) induced polarization electric fields during the midnight (postsunset) periods. When the background zonal electric field is also weak, the induced polarization charges will be further reduced causing significantly slower rise velocities around the midnight hours as seen in Figure 5a. This weak polarization electric fields within the bubble may also be responsible for lower H_m (Figure 5b). It is further understood that the EPBs cease to rise further when the ion density inside the bubble becomes equal to that of the nearby background. Using SAMI3 model simulation, *Krall et al.* [2010] confirmed that the EPB stops rising to higher altitudes when the flux-tube-integrated ion mass density inside the upper edge of the bubble is equal to that of the adjacent background. Therefore, the weak polarization electric fields within the bubble and the reduced background density during midnight hours cause the cessation of EPB growth at lower altitudes.

5. Conclusions

We have analyzed the altitude development and estimated the vertical rise velocities of freshly evolved EPBs over Kototabang using the two-dimensional backscatter maps of EAR during May 2010 to April 2013. Out of 86 EPBs 68 are from postsunset period and 18 EPBs were observed around midnight hours. The result shows a clear difference between the rise velocities of postsunset and midnight EPBs. The rise velocities of midnight EPBs are varying between ~26 and 128 m/s, whereas postsunset EPBs show a larger variability between ~45 and 265 m/s. The maximum altitude attained by the midnight EPBs are much lower compared to the postsunset EPBs. The majority of the postsunset EPBs reached the maximum detectable altitude of radar FOV. The estimated rise velocities from EAR observations were consistent with the nonlinear evolution of plasma bubbles simulated using the high-resolution bubble (HIRB) model. The controlled HIRB simulations with varying background electric field and local time conditions indicate that the rise velocity and the nonlinear evolution of EPB is mainly controlled by the background zonal electric field. Further, the reduced background ion density during midnight hours is also an important factor that causes significant reduction of the vertical rise velocity (V_r) and maximum attainable altitude (H_m) of EPBs through reduced polarization electric fields within the bubble and reduced density gradients with the adjacent regions.

Acknowledgments
The EAR data obtained from the PI, M. Yamamoto (yamamoto@rish.kyoto-u.ac.jp). The HIRB model is available at NICT, Japan with the PI, T. Yokoyama (tyoko@nict.go.jp).

References

Abdu, M. A., R. T. de Meiros, J. H. A. Sobrel, and J. A. Bittencourt (1983), Spread *F* plasma bubble vertical rise velocities determined from spaced ionosonde observations, *J. Geophys. Res.*, *88*, 9197–9204, doi:10.1029/JA088iA11p09197.

Ajith, K. K., S. Tulasi Ram, M. Yamamoto, T. Yokoyama, V. S. Gowtam, Y. Otsuka, T. Tsugawa, and K. Niranjan (2015), Explicit characteristics of evolutionary-type plasma bubbles observed from Equatorial Atmosphere Radar during the low to moderate solar activity years 2010–2012, *J. Geophys. Res. Space Physics*, *120*, 1371–1382, doi:10.1002/2014JA020878.

Ajith, K. K., S. Tulasi Ram, M. Yamamoto, Y. Otsuka, and K. Niranjan (2016), On the fresh development of equatorial plasma bubbles around the midnight hours of June solstice, *J. Geophys. Res. Space Physics*, *121*, 9051–9062, doi:10.1002/2016JA023024.

Anderson, D. N., and G. Haerendel (1979), The motion of depleted plasma regions in the equatorial ionosphere, *J. Geophys. Res.*, *84*, 4251–4256, doi:10.1029/JA084iA08p04251.

Basu, B., and B. Coppi (1999), Relevance of plasma and neutral wind profiles to the topology and the excitation of modes for the onset of equatorial spread *F*, *J. Geophys. Res.*, *104*, 225–231, doi:10.1029/1998JA900069.

Basu, S., et al. (1996), Scintillations, plasma drifts, and neutral winds in the equatorial ionosphere after sunset, *J. Geophys. Res.*, *101*(A12), 26,795–26,809, doi:10.1029/96JA00760.

Baumjohann, W., and R. A. Treumann (1997), *Basic Space Plasma Physics*, *World Scientific*, vol. 65, pp. 65–67, Imperial College Press, London.

Carter, B. A., E. Yizengaw, J. M. Retterer, M. Francis, M. Terkildsen, R. Marshall, R. Norman, and K. Zhang (2014), An analysis of the quiet time day-to-day variability in the formation of postsunset equatorial plasma bubbles in the Southeast Asian region, *J. Geophys. Res. Space Physics*, *119*, 3206–3223, doi:10.1002/2013JA019570.

Chandra, H., and R. G. Rastogi (1970), Solar cycle and seasonal variation of spread-*F* near the magnetic equator, *J. Atmos. Terr. Phys.*, *32*, 439–443.
Dabas, R. S., and B. M. Reddy (1990), Equatorial plasma bubble rise velocities in the Indian sector determined from multistation scintillation observations, *Radio Sci.*, *25*, 125–132, doi:10.1029/RS025i002p00125.
Dao, T., Y. Otsuka, K. Shiokawa, S. Tulasi Ram, and M. Yamamoto (2016), Altitude development of postmidnight F region field-aligned irregularities observed using Equatorial Atmosphere Radar in Indonesia, *Geophys. Res. Lett.*, *43*, 1015–1022, doi:10.1002/2015GL067432.
Fagundes, P. R., Y. Sahai, I. S. Batista, M. A. Abdu, J. A. Bittencourt, and H. Takahashi (1999), Observations of day-to-day variability in precursor signatures of equatorial *F*-region plasma depletions, *Ann. Geophys.*, *17*, 1053–1063.
Fejer, B. G., D. T. Farley, R. F. Woodman, and C. Calderon (1979), Dependence of equatorial *F* region vertical drifts on season and solar cycle, *J. Geophys. Res.*, *84*, 5792–5796, doi:10.1029/JA084iA10p05792.
Fejer, B. G., E. R. de Paula, S. A. Gonzalez, and R. F. Woodman (1991), Average vertical and zonal *F* region plasma drifts over Jicamarca, *J. Geophys. Res.*, *96*(A8), 13,901–13,906, doi:10.1029/91JA01171.
Fejer, B. G., L. Scherliess, and E. R. de Paula (1999), Effects of the vertical plasma drift velocity on the generation and evolution of equatorial spread-*F*, *J. Geophys. Res.*, *104*(A9), 19,859–19,869, doi:10.1029/1999JA900271.
Haerendel, G. (1973), Theory of Equatorial Spread F, Report, Max-Planck Inst. for Phys., and Astrophys, Garching, Germany.
Hargreaves, J. K. (1992), *The Solar-Terrestrial Environment*, vol. 244, pp. 243–247, Cambridge Univ. Press, Cambrige.
Keskinen, M. J., S. L. Ossakow, and B. G. Fejer (2003), Three-dimensional nonlinear evolution of equatorial ionospheric spread-*F* bubbles, *Geophys. Res. Lett.*, *30*(16), 1855, doi:10.1029/2003GL017418.
Krall, J., J. D. Huba, S. L. Ossakow, and G. Joyce (2010), Why do equatorial ionospheric bubbles stop rising?, *Geophys. Res. Lett.*, *37*, L09105, doi:10.1029/2010GL043128.
Ossakow, S. L., S. T. Zalesak, B. E. McDonald, and P. K. Chaturvedi (1979), Nonlinear equatorial spread *F*: Dependence on altitude of the *F* peak and bottomside background electron density gradient scale length, *J. Geophys. Res.*, *84*, 17–29, doi:10.1029/JA084iA01p00017.
Otsuka, Y., T. Ogawa, and Effendy (2009), VHF radar observations of nighttime *F*-region field-aligned irregularities over Kototabang, Indonesia, *Earth Planets Space*, *61*(4), 431–437.
Rama Rao, P. V. S., S. Gopi Krishna, K. Niranjan, and D. S. V. V. D. Prasad (2006), Study of spatial and temporal characteristics of L-band scintillations over the Indian low-latitude region and their possible effects on GPS navigation, *Ann. Geophys., EGU*, *24*(6), 1567–1580.
Sastri, J. H. (1999), Post-midnight onset of spread-*F* at Kodaikanal during the June solstice of solar minimum, *Ann. Geophys.*, *17*, 1111–1115.
Scannapieco, A. J., and S. L. Ossakow (1976), Nonlinear equatorial spread *F*, *Geophys. Res. Lett.*, *3*, 451–454, doi:10.1029/GL003i008p00451.
Stoneback, R. A., R. A. Heelis, A. G. Burrell, W. R. Coley, B. G. Fejer, and E. Pacheco (2011), Observations of quiet time vertical ion drift in the equatorial ionosphere during the solar minimum period of 2009, *J. Geophys. Res.*, *116*, A12327, doi:10.1029/2011JA016712.
Subbarao, K. S. V., and B. V. Krishna Murthy (1994), Post-sunset *F* region vertical velocity variations at magnetic equator, *J. Atmos. Terr. Phys.*, *56*, 59–65.
Sultan, P. J. (1996), Linear theory and modeling of the Rayleigh-Taylor instability leading to the occurrence of equatorial spread F, *J. Geophys. Res.*, *101*(A12), 26875–26891, doi:10.1029/96JA00682.
Tsunoda, R. T. (1981), Time evolution and dynamics of equatorial backscatter plumes 1. Growth phase, *J. Geophys. Res.*, *8*(A1), 139–149, doi:10.1029/JA086iA01p00139.
Tsunoda, R. T. (1985), Control of the seasonal and longitudinal occurrence of equatorial scintillations by the longitudinal gradient in integrated *E* region Pedersen conductivity, *J. Geophys. Res.*, *90*, 447–456, doi:10.1029/JA090iA01p00447.
Tsunoda, R. T. (2005), On the enigma of day-to-day variability in equatorial spread *F*, *Geophys. Res. Lett.*, *32*, L08103, doi:10.1029/2005GL022512.
Tsunoda, R. T., and B. R. White (1981), On the generation and growth of equatorial backscatter plumes: 1. Wave structure in the bottomside *F* layer, *J. Geophys. Res.*, *86*, 3610–3616, doi:10.1029/JA086iA05p03610.
Tsunoda, R. T., M. Yamamoto, T. Tsugawa, T. L. Hoang, S. Tulasi Ram, S. V. Thampi, H. D. Chau, and T. Nagatsuma (2011), On seeding, large-scale wave structure, equatorial spread *F*, and scintillations over Vietnam, *Geophys. Res. Lett.*, *38*, L20102, doi:10.1029/2011GL049173.
Tsunoda, R. T., R. C. Livingston, J. P. McClure, and W. B. Hanson (1982), Equatorial plasma bubbles: Vertically elongated wedges from the bottomside *F* layer, *J. Geophys. Res.*, *87*(A11), 9171–9180, doi:10.1029/JA087iA11p09171.
Tulasi Ram, S., M. Yamamoto, R. T. Tsunoda, H. D. Chau, T. L. Hoang, B. Damtie, M. Wassaie, C. Y. Yatini, T. Manik, and T. Tsugawa (2014), Characteristics of large scale wave structure observed from African and Southeast Asian longitudinal sectors, *J. Geophys. Res. Space Physics*, *119*, 2288–2297, doi:10.1002/2013JA019712.
Tulasi Ram, S., P. V. S. Rama Rao, K. Niranjan, D. S. V. V. D. Prasad, R. Sridharan, C. V. Devasia, and S. Ravindran (2006), The role of post-sunset vertical drifts at the equator in predicting the onset of VHF scintillations during high and low sunspot activity years, *Ann. Geophys.*, *24*, 1609–1616.
Tulasi Ram, S., M. Yamamoto, R. T. Tsunoda, S. V. Thampi, and S. Gurubaran (2012), On the application of differential phase measurements to study the zonal large scale wave structure (LSWS) in the ionospheric electron content, *Radio Sci.*, *47*, RS2001, doi:10.1029/2011RS004870.
Yizengaw, E., J. Retterer, E. E. Pacheco, P. Roddy, K. Groves, R. Caton, and P. Baki (2013), Postmidnight bubbles and scintillations in the quiet-time June solstice, *Geophys. Res. Lett.*, *40*, 5592–5597, doi:10.1002/2013GL058307.
Yokoyama, T., and S. Fukao (2006), Upwelling backscatter plumes in growth phase of equatorial spread F observed with the Equatorial Atmosphere Radar, *Geophys. Res. Lett.*, *33*, L08104, doi:10.1029/2006GL025680.
Yokoyama, T., H. Shinagawa, and H. Jin (2014), Nonlinear growth, bifurcation, and pinching of equatorial plasma bubble simulated by three-dimensional high-resolution bubble model, *J. Geophys. Res. Space Physics*, *119*, 10,474–10,482, doi:10.1002/2014JA020708.
Yokoyama, T., R. F. Pfaff, M. Yamamoto, Y. Otsuka, M. Nishioka, and T. Tsugawa (2011a), On postmidnight low-latitude ionospheric irregularities during solar minimum: 1. Equatorial Atmosphere Radar and GPS TEC observations in Indonesia, *J. Geophys. Res.*, *116*, A11325, doi:10.1029/2011JA016797.
Yokoyama, T., R. F. Pfaff, P. A. Roddy, M. Yamamoto, and Y. Otsuka (2011b), On post-midnight low-latitude ionospheric irregularities during solar minimum: 2. C/NOFS observations and comparison with Equatorial Atmosphere Radar, *J. Geophys. Res.*, *116*, A11326, doi:10.1029/2011JA016798.

Erratum

In the originally published version of this article, Figure 2 reported an inaccurate mean vertical rise velocity. The figure has since been corrected, and the current version may be considered the authoritative version of record.